Journal of Solid State Chemistry 184 (2011) 563–571

Contents lists available at ScienceDirect

Journal of Solid State Chemistry

journal homepage: www.elsevier.com/locate/jssc

Visible and infrared luminescence properties of Er^{3+}-doped $Y_2Ti_2O_7$ nanocrystals

Chu-Chi Ting*, Yi-Shan Chiu, Chia-Wei Chang, Liang-Chih Chuang

Graduate Institute of Opto-Mechatronics Engineering, National Chung Cheng University, 168 University Rd., Min-Hsiung, Chia-Yi, Taiwan, ROC

ARTICLE INFO

Article history:
Received 2 July 2010
Received in revised form
10 December 2010
Accepted 2 January 2011
Available online 13 January 2011

Keywords:
Erbium
Upconversion
PL
Pyrochlore
Lifetime

ABSTRACT

Er^{3+}-doped $Y_2Ti_2O_7$ nanocrystals were fabricated by the sol–gel method. While the annealing temperature exceeds 757 °C, amorphous pyrochlore phase $Er_xY_{2-x}Ti_2O_7$ transfers to well-crystallized nanocrystals, and the average crystal size increases from ~70 to ~180 nm under 800–1000 °C/1 h annealing. $Er_xY_{2-x}Ti_2O_7$ nanocrystals absorbing 980 nm photons can produce the upconversion (526, 547, and 660 nm; $^2H_{11/2}\rightarrow{}^4I_{15/2}$, $^4S_{3/2}\rightarrow{}^4I_{15/2}$, and $^4F_{9/2}\rightarrow{}^4I_{15/2}$, respectively) and Stokes (1528 nm; $^4I_{13/2}\rightarrow{}^4I_{15/2}$) photoluminescence (PL). The infrared PL decay curve is single-exponential for Er^{3+} (5 mol%)-doped $Y_2Ti_2O_7$ nanocrystals but slightly nonexponential for Er^{3+} (10 mol%)-doped $Y_2Ti_2O_7$ nanocrystals. For 5 and 10 mol% doping concentrations, the mechanism of up-converted green light is the two-photon excited-state absorption. Much stronger intensity of red light relative to green light was observed for the sample with 10 mol% dopant. This phenomenon can be attributed to the reduced distance between Er^{3+}–Er^{3+} ions, resulting in the enhancement of the energy-transfer upconversion and cross-relaxation mechanisms.

1. Introduction

Erbium-doped materials have been extensively utilized in the optical communication system because the Er^{3+} ions excited by 980 nm photons can emit ~1.54 μm photons which are in the region of the optimum transmission of silica-based glass fibers [1]. Additionally, erbium-doped materials also have the good upconversion (UC) property for the application in upconversion lasers [2]. In recent years, the erbium-doped materials have attracted the specific attention on the application of the luminescent solar converter (LSC) because of the visible (Vis) upconversion property [3–6]. Generally, LSC is a transparent organic or ceramic fluorescent thin film which is doped or blended by organic dyes [7], rare-earth (Re) activators [8], silicon nanocrystals [9], or quantum dots [10,11] on the top or bottom of solar cells. It can absorb the ultraviolet (UV) light and emit the Vis light by the downconversion mechanism, or absorb the infrared (IR) light and emit the Vis light by the upconversion mechanism [12]. Shalav et al. [4] reported that the silicon solar cell in combination with the $NaYF_4$:Er^{3+} UC-phosphors gave an external quantum efficiency close to $2.5\pm0.2\%$ under 5.1 mW laser excitation at 1523 nm.

Basically, the multiphonon relaxation process is directly related to the phonon energy of host materials, which can considerably influence the photoluminescence (PL) properties [13]. Low phonon-energy materials such as Y_2O_3 [14,15], Gd_2O_3 [16,17], ZrO_2 [18,19], and $YAlO_3$ [20,21] prevent the de-excitation of the excited-state levels through the nonradiative phonon-assisted relaxation, resulting in the strongly enhanced luminescence intensity for the IR-to-Vis upconversion. Pyrochlore-phase dititanate $Y_2Ti_2O_7$ possesses a face-centered cubic crystal structure with the space group *Fd*3*m* (lattice constant, $a=10.09$ nm) [22,23], high refractive index (2.34 at $\lambda=563$ nm) [24], high optical band gap (~3.7 eV) [25,26], and low phonon energy ($<712\ cm^{-1}$) [27]. Because Y^{3+} and Er^{3+} ions have similar ionic radii ($Y^{3+}=0.0892$ nm and $Er^{3+}=0.0881$ nm), as well as $Y_2Ti_2O_7$ and $Er_2Ti_2O_7$ have the same crystal structural and similar lattice constant, Er^{3+} ions can replace Y^{3+} ions in the $Y_2Ti_2O_7$ lattice, implying that both Y^{3+} and Er^{3+} ions in Er^{3+}-doped $Y_2Ti_2O_7$ are structurally indistinguishable. Therefore, $Y_2Ti_2O_7$ is a very good candidate for Er^{3+} doping, and Er^{3+} ions should distribute very well in the $Y_2Ti_2O_7$ lattice, resulting in the reduction of the concentration quenching effect and the increase of the PL intensity. Additionally, the $Y_2Ti_2O_7$ host possessing lower phonon energy than do silica-based glasses can reduce the possibility of nonradiative recombination and increase the upconversion luminescence intensity of Er^{3+} ions.

In this paper, Er^3-doped $Y_2Ti_2O_7$ nanocrystals were fabricated by the sol–gel method which is a very easy technique to fabricate

* Corresponding author. Fax: +886 5 2724036.
E-mail address: ccting@ccu.edu.tw (C.-C. Ting).

0022-4596/$ - see front matter © 2011 Elsevier Inc. All rights reserved.
doi:10.1016/j.jssc.2011.01.001

nanocrystals with homogeneous dispersion and the precisely desired stoichiometry of dopants. We demonstrate that Er^{3+} (3, 5, 7, or 10 mol%)-doped $Y_2Ti_2O_7$ (i.e., $Er_xY_{2-x}Ti_2O_7$, $x=0.03$, 0.05, 0.07, or 0.1) nanocrystals have the good upconversion and Stokes PL properties. The effects of Er^{3+} doping concentration and annealing temperature on the phase development, crystal structure, and related upconversion luminescence mechanisms of Er^{3+}-doped $Y_2Ti_2O_7$ nanocrystals will be systematically investigated.

2. Experimental materials and methods

Acetic acid (HAc, CH_3COOH, 99.5%, Merck) and 2-methoxyethanol (2-MOE, $HOC_2H_4OCH_3$, 99.5%, Merck) with the molar ratio of Ti/HAc/2-MOE=1/10/15 were first dropped to titanium isoproxide {$Ti[OCH(CH_3)_2]_4$, ≧98%, Acros} to form the titanium solution. Subsequently, yttrium solution {a mixture of yttrium acetate [$Y(CH_3COO)_3\cdot 4H_2O$, 99.9%, Alfa], methanol (Me, CH_3OH, ≧99.5%, Merck), and ethylene glycol (EG, $HOCH_2CH(OH)CH_2OH$, ≧99.5%, Alfa) with the molar ratio of Y/Me/EG=1/49/10} and erbium acetate [$Er(CH_3COO)_3\cdot 4H_2O$, 99.9%, Alfa] were added to the titanium solution, followed by stirring for 10 h in order to process homogeneous hydrolysis and polymerization reaction for the formation of the Er^{3+} (0, 3, 5, 7, or 10 mol%)-doped $Y_2Ti_2O_7$ sol–gel solution.

Finally, the Er^{3+} (0, 3, 5, 7, or 10 mol%)-doped $Y_2Ti_2O_7$ sol–gel solutions were aged at room temperature for 2 days and then heat-treated at 100 °C in air for 2 days in order to get pink transparent dried gels. Dried gels were pyrolyzed at 700–1000 °C for 1 h in air atmosphere at a rate of 5 °C h^{-1} to remove organic species. Pyrolyzed gel powders were die-pressed by a hydraulic press at 5 MPa to be 1-cm-diameter and 2-mm-thick pellets for the further measurements of structural and PL characterizations.

The thermal decomposition of Er^{3+}-doped $Y_2Ti_2O_7$ xerogel powders was studied by a thermogravimetric analysis (TGA, TA Instrument 5100) and differential scanning calorimetry (DSC, Netzsch Instrument HT-DSC404) from 30 to 1000 °C with a heating rate of 3 °C/min in air flow. The X-ray diffraction (XRD) measurement of samples was performed by an X-ray diffractometer (Shimadzu XRD 6000) with Cu$K\alpha$ radiation ($\lambda=0.154$ nm). Scanning electron microscope (Hitachi, S4800-I) was operated at an accelerating voltage of 15 kV for the microstructural examination. A 980 nm diode laser (JDSU, S26-7602-300, maximum power 300 mW) was inclined 45° and focused to irradiate the center of pallets with a spot of ~1 mm. Fluorescence spectra were recorded normally from pallets by using a spectrophotometer (Horiba Jobin-yvon, iHR 550) equipped with a InGaAs photodiode (Electro-Optical Systems Inc., IGA-050-TE2-H) and photomultiplier tube (Hamamatasu, 7732 P-01) at room temperature, and the distance between pallets and spectrophotometer was accurately fixed for each measurement. The response of the detection system was precisely calibrated with a tungsten wire calibration source. The decay curves of Vis and IR emissions were obtained by modulating the 980 nm laser at 15 Hz with a chopper, and the outputs of the photomultiplier tube and InGaAs photodiode were recorded by a digital oscilloscope (Tektronix, DPO 3032).

3. Results and discussion

3.1. Crystal structure

Fig. 1 shows the TGA and DSC curves of Er^{3+} (5 mol%)-doped $Y_2Ti_2O_7$ xerogel powders. The TGA curve shows a significant weight loss in the temperature range from room temperature (RT) to 757 °C. A significant weight loss is observed below 350 °C due to the evaporation of physically adsorbed water and residual organic solvents. The weight loss corresponding to the decomposition/combustion of organic components and the formation of amorphous pyrochlore phase is at the temperature range of 350–725 °C. The crystallization of amorphous pyrochlore phase occurs at 725–757 °C. A slight increase in mass (1.3%) between 440 and 572 °C could be due to the additional pick-up CO_2 from the atmosphere [28]. No weight loss was observed as the sample was heated over 757 °C, which implies that the thermally stabilized and well-crystallized pyrochlore phase Er^{3+} (5 mol%)-doped $Y_2Ti_2O_7$ nanocrystals had formed. In addition, it can be seen that a weak endothermal peak at 335 °C is ascribed to the evaporation of physically adsorbed water and a weak exothermal peak at 757 °C is related to the crystallization of the amorphous pyrochlore phase in the DSC curve.

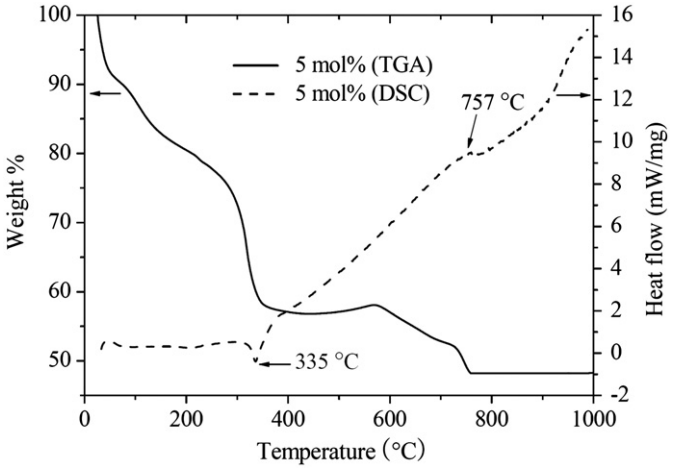

Fig. 1. TGA and DSC curves of Er^{3+} (5 mol%)-doped $Y_2Ti_2O_7$ xerogel powders.

The X-ray diffraction (XRD) patterns in Fig. 2(a) and (b) show the effect of the annealing temperature on the phase evolution of Er^{3+} (5 or 10 mol%)-doped $Y_2Ti_2O_7$ nanocrystals. Obviously, a weak broad continuum around $2\theta=\sim 30^\circ$ in the XRD patterns is the characteristic of an amorphous structure for the samples annealed at 600 and 700 °C. While the annealing temperature exceeds 800 °C, the well-crystallized pyrochlore phase is identified by the characteristic XRD peaks: (2 2 2), (4 0 0), (4 4 0), and (6 2 2) [29]. On the other hand, other samples [Er^{3+} (3 or 7 mol%)-doped $Y_2Ti_2O_7$] also exhibit the same effect of the annealing temperature on the phase evolution and the XRD patterns are similar to Fig. 2(a) and (b) (not shown here). All the XRD patterns indicate the formation of only a single pyrochlore phase without any possible other phases such as TiO_2 (rutile phase), Y_2O_3, and Er_2O_3.

Fig. 2(c) and (d) shows the XRD patterns of the Er^{3+} (3, 5, 7, or 10 mol%)-doped $Y_2Ti_2O_7$ nanocrystals annealed at 800 or 1000 °C for 1 h. All of the samples possess the pyrochlore structure. Compared to the diffraction intensities of all the XRD peaks between samples, the addition of 3–10 mol% Er^{3+} ions does not significantly influence the peak intensities of $Er_xY_{2-x}Ti_2O_7$ nanocrystals, which means that the addition of 3–10 mol% Er^{3+} ions into $Y_2Ti_2O_7$ host does not apparently degrade the crystallinity of $Er_xY_{2-x}Ti_2O_7$ nanocrystals.

The average grain size (D) of $Er_xY_{2-x}Ti_2O_7$ nanocrystals is determined by the Scherrer equation [30]

$$D=\frac{S\lambda}{\sqrt{B_M^2-B_S^2}\cos\theta} \quad (1)$$

where S is the Scherrer constant (0.9), λ is the wavelength of incident radiation, θ is the Bragg angle corresponding to the XRD peak being considered, as well as B_M and B_S are the width in radians of one of the sample and standard (Si powder) diffraction

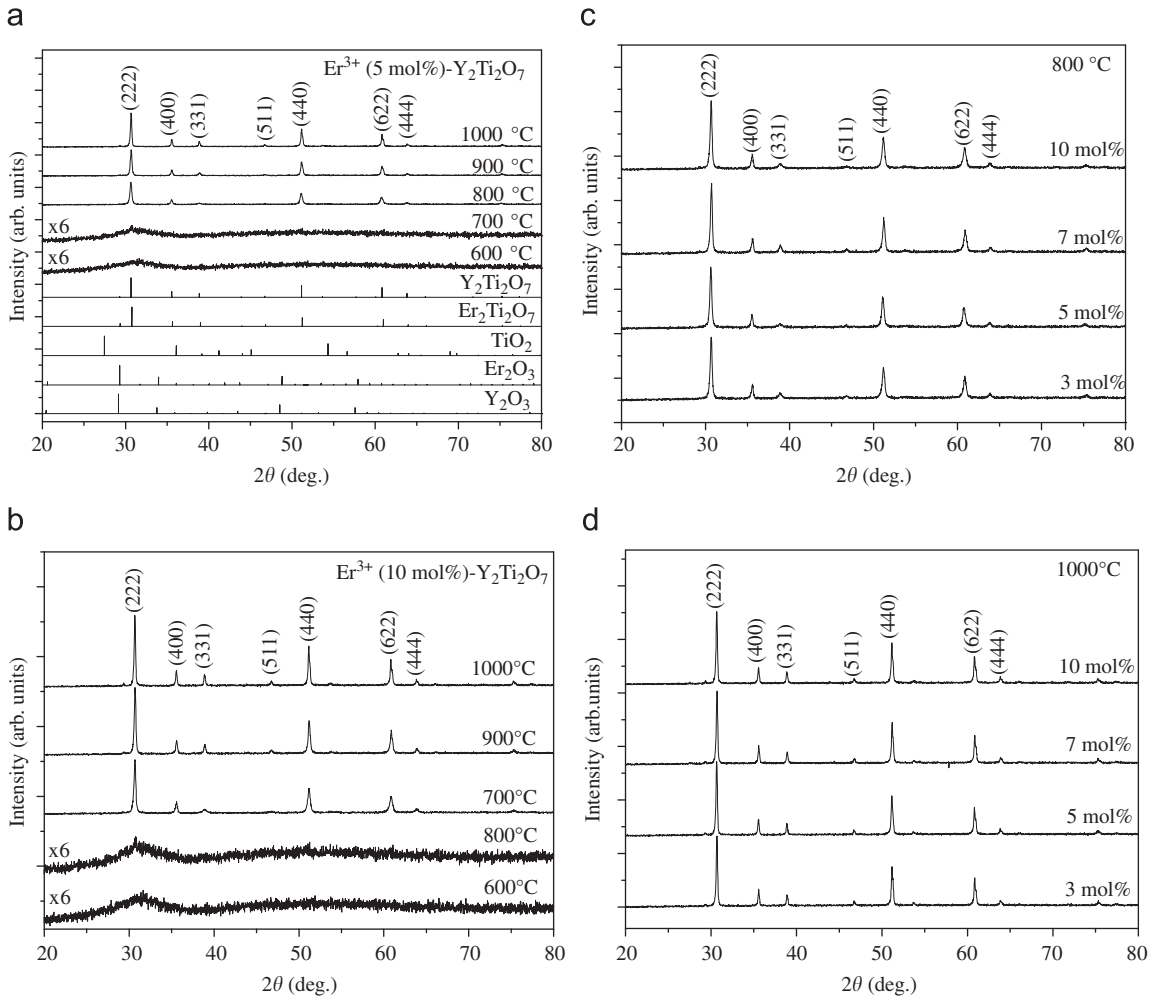

Fig. 2. XRD patterns of (a) Er^{3+} (5 mol%)-doped $Y_2Ti_2O_7$ nanocrystals annealed at 600–1000 °C for 1 h, (b) Er^{3+} (10 mol%)-doped $Y_2Ti_2O_7$ nanocrystals annealed at 600–1000 °C for 1 h, (c) Er^{3+} (3, 5, 7, or 10 mol%)-doped $Y_2Ti_2O_7$ nanocrystals annealed at 800 °C for 1 h and (d) Er^{3+} (3, 5, 7, or 10 mol%)-doped $Y_2Ti_2O_7$ nanocrystals annealed at 1000 °C for 1 h. The 2θ positions for bulk $Y_2Ti_2O_7$, $Er_2Ti_2O_7$, TiO_2 (rutile phase), Y_2O_3, and Er_2O_3 are shown on the plot for the reference.

peaks at half-maximum, respectively. The instrument broadening (B_S) is 0.14 in our system. The average estimated grain sizes of the Er^{3+} (5 mol%)-doped $Y_2Ti_2O_7$ nanocrystals annealed at 800, 900, and 1000 °C for 1 h are ~44, ~54, and ~76 nm, respectively. On the other hand, estimated crystal sizes of the Er^{3+} (3, 7, or 10 mol%)-doped $Y_2Ti_2O_7$ nanocrystals annealed at 800–1000 °C for 1 h also exhibit the similar values, which implies that the addition of 3–10 mol% Er^{3+} ions into $Y_2Ti_2O_7$ host does not apparently influence the grain size of $Er_xY_{2-x}Ti_2O_7$ nanocrystals.

Fig. 3(a)–(f) illustrates the top-view scanning electron microscopy (SEM) imagines of the Er^{3+} (5 or 10 mol%)-doped $Y_2Ti_2O_7$ nanocrystals annealed at 800, 900, and 1000 °C for 1 h. For the samples annealed below 800 °C, no crystal image is detected because of the amorphous structure, indicating that image resolution is beyond the detective limitation of the scanning electron microscope. As the annealing temperature increases to 800 °C, Er^{3+} (5 or 10 mol%)-doped $Y_2Ti_2O_7$ nanocrystals have the average grain size of approximately 70 nm. Further, the average grain size gradually increases to ~90 and ~180 nm at 900 and 1000 °C annealing, respectively. The evolution of the microstructure for the Er^{3+} (3 or 7 mol%)-doped $Y_2Ti_2O_7$ nanocrystals annealed at 800–1000 °C is also similar to that of Er^{3+} (5 or 10 mol%)-doped $Y_2Ti_2O_7$ nanocrystals (SEM images not shown here). SEM images disclose again that the evolution of grain size for the Er^{3+}-doped $Y_2Ti_2O_7$ nanocrystals annealed at different temperatures has the same trend as that detected by the FWHM of the XRD peak. However, the FWHM of the XRD peak can be widened by internal stress and defects so the mean grain size estimated by Scherrer's equation is normally smaller than the real value. In addition, when the grain size is larger than 100 nm, Scherrer's equation cannot be used to determine the average grain size because of the limitation of diffractometer resolution. The discrepancy of average estimated grain size can be obviously observed in the SEM images.

The above-mentioned evolutions of the XRD peak intensities and crystal sizes of the Er^{3+} (3, 5, 7, or 10 mol%)-doped $Y_2Ti_2O_7$ nanocrystals annealed at 800–1000 °C obviously appear to be very similar. Er^{3+} ions can replace the positions of Y^{3+} ions in the $Y_2Ti_2O_7$ lattice because Y^{3+}/Er^{3+} ions have the same valance electrons and similar ionic radii as well as $Y_2Ti_2O_7/Er_2Ti_2O_7$ have the same crystal structural and similar lattice constant. Therefore, Y^{3+} and Er^{3+} ions are structurally undistinguished in the $Er_xY_{2-x}Ti_2O_7$ lattice, which results in the very similar properties on the phase evolution and crystal growth for Er^{3+} (3, 5, 7, or 10 mol%)-doped $Y_2Ti_2O_7$ nanocrystals.

3.2. Optical properties

3.2.1. Vis–IR photoluminescence

Fig. 4(a) and (b) shows the upconversion and Stokes PL spectra of the Er^{3+} (5 mol%)-doped $Y_2Ti_2O_7$ nanocrystals annealed at 600–1000 °C for 1 h and the Er^{3+} (3, 5, 7, or 10 mol%)-doped $Y_2Ti_2O_7$ nanocrystals annealed at 800 °C for 1 h excited by

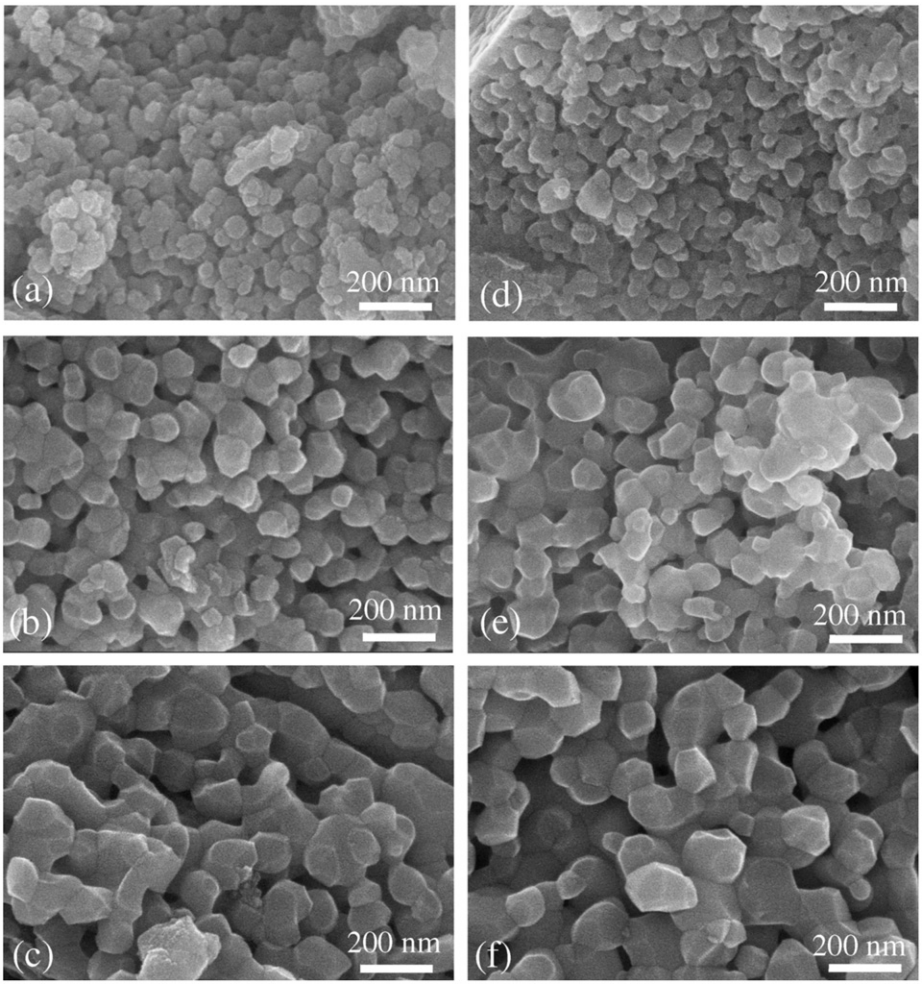

Fig. 3. Top-view SEM imagines of Er^{3+} (5 mol%)-doped $Y_2Ti_2O_7$ nanocrystals annealed at (a) 800, (b) 900, and (c) 1000 °C for 1 h and Er^{3+} (10 mol%)-doped $Y_2Ti_2O_7$ nanocrystals annealed at (d) 800, (e) 900 and (f) 1000 °C for 1 h.

980 nm, respectively. These visible to infrared fluorescence spectra exhibit the bands at about 526, 547, 660, and 1528 nm which are identified as the $^2H_{11/2}\rightarrow{}^4I_{15/2}$, $^4S_{3/2}\rightarrow{}^4I_{15/2}$, $^4F_{9/2}\rightarrow{}^4I_{15/2}$, and $^4I_{13/2}\rightarrow{}^4I_{15/2}$ transitions, respectively. Although $Er_xY_{2-x}Ti_2O_7$ nanocrystals possessing lower phonon energy could induce UV and blue upconversion luminescence, no UV and blue light can be detected in our measurement system. This could be attributed to the very weak intensity of UV and blue upconversion luminescence which cannot be detected due to the limitation of our existing experimental set-up. Or the nanocrystalline materials possess lots of absorbed contaminants (e.g., CO_3^- and OH^-) on the surface and lattice defects, which results in the enhancement of nonradiative multiphonon decay and no UV/blue upconversion luminescence [14]. Therefore, this paper only focuses on the study of green, red, and infrared emissions of $Er_xY_{2-x}Ti_2O_7$ nanocrystals. However, the more detailed UV–Vis fluorescence measurement will be executed by more delicate equipments in the near future.

The effect of the annealing temperature on the evolutions of Vis and IR PL intensities and spectral shapes of Er^{3+} (3, 7, or 10 mol%)-doped $Y_2Ti_2O_7$ nanocrystals are similar to the case of Er^{3+} (5 mol%)-doped $Y_2Ti_2O_7$ nanocrystals (PL spectra not shown here). Obviously, 5 mol% and 800 °C are the optimum Er^{3+} doping concentration and annealing temperature for $Er_xY_{2-x}Ti_2O_7$ system to achieve the maximum PL intensity, respectively. A broaden Vis and IR PL spectra consisting of some main peaks at 526, 547, 660, and 1528 nm were observed in the sample annealed at 600 and 700 °C/1 h. Such broadband emissions indicate that the bonding environment of Er^{3+} ions obviously has wider diversity because of the amorphous structure. When the annealing temperature is higher than 800 °C, the shapes of Vis and IR PL spectra obviously split into some sharp peaks (Stark-splitting effect), implying that Er^{3+} ions locate on the well-defined lattice sites in the crystalline pyrochlore phase $Er_{0.05}Y_{1.95}Ti_2O_7$.

It is found from Fig. 4(a) that the Vis and IR PL intensities increase first with the increase of the annealing temperature from 600 to 700 °C (i.e., the temperature range of the formation of amorphous $Er_xY_{2-x}Ti_2O_7$), reach the maximum at 800 °C (i.e., the temperature range of the formation of crystalline $Er_xY_{2-x}Ti_2O_7$), and then decrease with increasing the annealing temperature from 900 to 1000 °C (i.e., the temperature range of the increase in the crystallinity of $Er_xY_{2-x}Ti_2O_7$). It is well known that the ~1.54 μm intra-4*f*–*f* transition is electric dipole forbidden for a free Er^{3+} ion. If the symmetry of the local crystal field at Er^{3+} lattice sites is distorted in host materials, the parity forbidden intra-4*f* transition will be partially allowed. In the well-crystallized $Y_2Ti_2O_7$ lattice, Y^{3+} ions are eight-coordinated in a distorted cubic coordination polyhedron with the D_{3d} symmetry containing the inversion center [22,23]. In addition, surface and lattice defects in Er^{3+}-doped $Y_2Ti_2O_7$ nanocrystals can increase the absorption of H_2O and CO_2 from air. These high phonon-energy carbonate (CO_3^-) and hydroxyl (OH^-) groups (i.e., ~3350 cm^{-1} for CO_3^- and ~1500 cm^{-1} for OH^-) can increase the opportunity of the nonradiative transition [31,32]. Therefore, the effect of quenching

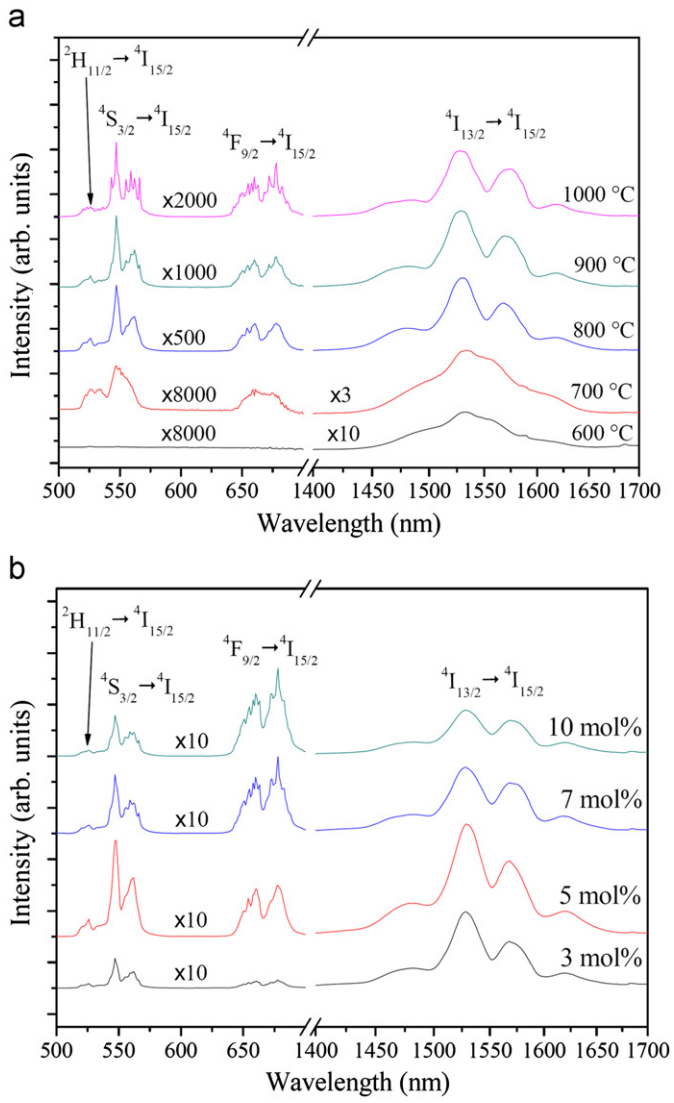

Fig. 4. Upconversion and Stokes PL spectra of (a) Er^{3+} (5 mol%)-doped $Y_2Ti_2O_7$ nanocrystals annealed at 600–1000 °C for 1 h, and (b) Er^{3+} (3, 5, 7, or 10 mol%)-doped $Y_2Ti_2O_7$ nanocrystals annealed at 800 °C for 1 h under 980 nm pumping.

centers (CO_3^- and OH^-) and the local symmetry of Er^{3+} lattice sites always compete with each other to influence the PL intensity.

Although the well-crystallized $Er_xY_{2-x}Ti_2O_7$ nanocrystals form at ≧800 °C annealing and Er^{3+} ions should locate on the well-defined lattice sites with high symmetry, the amount of hydroxyl quenching centers in the $Er_xY_{2-x}Ti_2O_7$ nanocrystals annealed at ≧800 °C is lower than that of the $Er_xY_{2-x}Ti_2O_7$ nanocrystals annealed at ≦700 °C (FTIR spectra not shown here). High temperature annealing can reduce the defects and impurities (CO_3^- and OH^-) of Er^{3+}-doped $Y_2Ti_2O_7$ nanocrystals, which results in the decrease of quenching centers and increase of PL intensity [14,33,34]. However, high temperature annealing can also improve the crystallinity and the local symmetry of Er^{3+} lattice sites, which leads to the reduction of PL intensity. Because the effect of increased local symmetry is counteracted by the effect of reduced quenching centers, the optimum annealing temperature is just located at 800 °C for Er^{3+}-doped $Y_2Ti_2O_7$ nanocrystals.

On the other hand, in Fig. 4(b), when Er^{3+} doping concentration is ≧7 mol% (i.e., ≧1.09×10^{21} ions/cm^3), the decrease of 1528 nm PL intensity indicates that the concentration quenching and cooperative upconversion effects are enhanced due to the reduced average spatial distance between Er^{3+} ions. In $Y_2Ti_2O_7$ there are eight molecules per unit cell, and the possible Y^{3+} sites for Er^{3+} ions to replace are 16. If we postulate that all Er^{3+} ions homogeneously distribute in the $Y_2Ti_2O_7$ lattice for the Er^{3+} doping concentration of 1.09×10^{21} ions/cm^3, the mean Er^{3+}–Er^{3+} distance is approximately 1.027 nm. This quenching concentration (1.09×10^{21} ions/cm^3) is larger than that of the traditional Er^{3+}-doped SiO_2 films [35,36].

3.2.2. Photoluminescence lifetime

Fig. 5(a)–(c) shows the 547, 660, and 1528 nm PL decay curves of the Er^{3+} (3, 5, 7, or 10 mol%)-doped $Y_2Ti_2O_7$ nanocrystals annealed at 800 °C for 1 h under the excitation of 980 nm. For 3, 5, 7, and 10 mol% Er^{3+} doping concentrations the lifetimes of 1528 nm PL are 6.66, 4.50, 4.40, and 2.86 ms, respectively, which are similar to the reported values [37–39]. The 1528 nm PL decay curves of (3, 5, or 7 mol%)-doped $Y_2Ti_2O_7$ nanocrystals are single-exponential; however, the decay curve slightly deviates from single exponentiality for (10 mol%)-doped $Y_2Ti_2O_7$ nanocrystals. This means that for 3–7 mol% Er^{3+} doping concentrations most Er^{3+} ions are situated in similar sites. For 10 mol% Er^{3+} doping concentration, some Er^{3+} ions on the nanoparticle surface absorbing lots of CO_3^- and OH^- quenching centers have faster decay than do those Er^{3+} ions located inside nanocrystals. The local environment of the Er^{3+} ions located close to the nanoparticle surface is different from that of those ions located inside nanocrystals, which leads to the reduced lifetime and slightly non-exponential decay curve. In addition, the enhanced energy-transfer mechanism between Er^{3+}–Er^{3+} ions also can significantly reduce the lifetime of the sample with 10 mol% Er^{3+} doping concentration.

The lifetimes of 547 nm upconversion emissions are all around 715 μs for the samples with 3, 5, 7, or 10 mol% Er^{3+} doping concentration, and the decay curves of all samples are single-exponential. The energy gap ΔE between $^2H_{11/2}/^4S_{3/2}$, and $^4F_{9/2}$ levels is about 3100 cm^{-1}, and only one OH^- phonon can bridge this energy gap. Therefore, the presence of adsorbants on the nanocrystalline surface leads to a more efficient depopulation for $^2H_{11/2}$ and $^4S_{3/2}$ levels of Er^{3+} ions on surface. This implies that the Er^{3+} ions on surface could not dominate the green upconversion and the green upconversion mainly may come from the Er^{3+} ions inside nanocrystals. In addition, the single-exponential decay curves for all samples indicate that the chemical environment of most Er^{3+} ions for Er^{3+} (3–10 mol%)-doped $Y_2Ti_2O_7$ nanocrystals are similar. In the other words, for the sample with 10 mol% Er^{3+} ions a certain proportion of Er^{3+} ions on the surface of nanocrystals could encounter the depopulation of $^2H_{11/2}$ and $^4S_{3/2}$ levels by multiphonon relaxation. Therefore, Er^{3+} (10 mol%)-doped $Y_2Ti_2O_7$ nanocrystals exhibit the single-exponential decay curve, which may be caused from the Er^{3+} ions inside nanocrystals.

The lifetimes of 660 nm upconversion emissions are 832, 895, 980, and 872 μs for the samples with 3, 5, 7, or 10 mol% Er^{3+} doping concentration, respectively, and the decay curves of all samples are also single-exponential. Compared to 547 nm emission, the longer lifetime could be attributed to the different energy-transfer upconversion and cross-relaxation mechanisms between green and red emissions [14], which will be discussed later. In addition, it is interesting to notice that the lifetime of red upconversion emission does not decrease monotonically with the increase in Er^{3+} doping concentration in comparison with that of the Stokes emission, and this is different from the case of the Er^{3+}-doped Y_2O_3 nanocrystals [14]. The detailed study on the temporal behavior of the upconversion lifetime versus Er^{3+} doping concentration will be examined by utilizing pulsed laser, and it'll be discussed on the separate paper in the future.

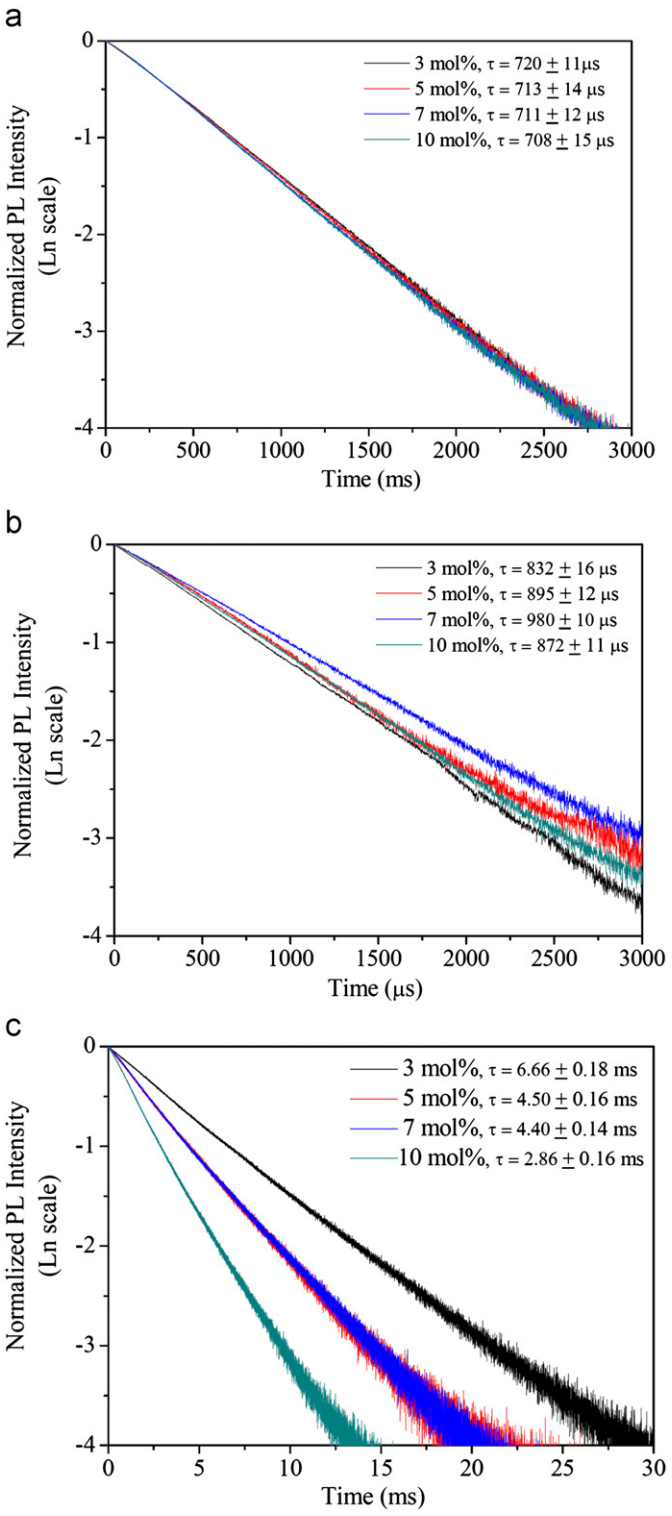

Fig. 5. (a) 547 (b) 660, and (c) 1528 nm PL decay curves of Er^{3+} (3, 5, 7, or 10 mol%)-doped $Y_2Ti_2O_7$ nanocrystals annealed at 800 °C for 1 h excited by 980 nm.

3.2.3. Upconversion mechanism

It is worthwhile to mention that the intensity of red emission increases with the increase of Er^{3+} doping concentration in upconversion luminescence spectra. Fig. 6(a) and (b) shows the intensity ratio of I_R/I_G and $(I_G+I_R)/I_{IR}$ as a function of dopant concentration in Er^{3+}-doped $Y_2Ti_2O_7$ nanocrystals, respectively (where I_G, I_R, and I_{IR} represent the integrated intensity of green,

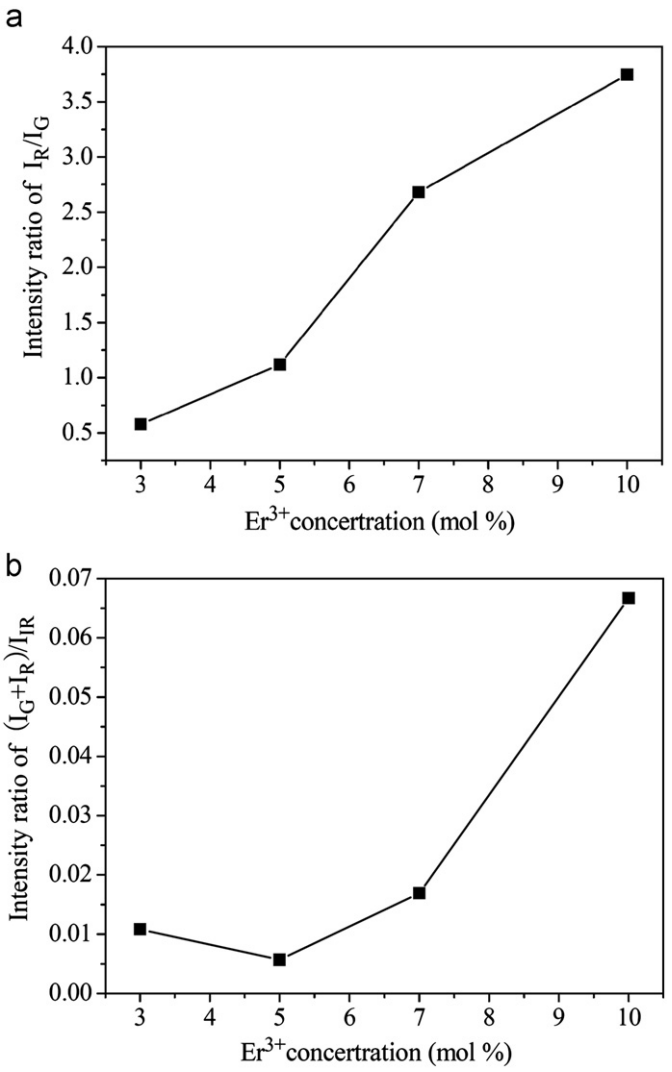

Fig. 6. Intensity ratio of (a) I_R/I_G and (b) $(I_G+I_R)/I_{IR}$ as a function of dopant concentrations for Er^{3+}-doped $Y_2Ti_2O_7$ nanocrystals (where I_G, I_R, and I_{IR} represent the intensity of green, red, and IR emissions, respectively).

red, and IR emissions, respectively). By increasing Er^{3+} doping concentration from 3 to 10 mol%, the relative intensity ratio (I_R/I_G) of red and green upconversion luminescence increase from ~0.58 to an approximately value of 3.75. The energy gap ΔE between the $^4S_{3/2}$ and $^4F_{9/2}$ levels is about 3100 cm^{-1}, and it requires at least five phonons ($Y_2Ti_2O_7$, cutoff energy = ~714 cm^{-1}) to bridge this energy gap. Hence, the nonradiative relaxation from $^4S_{3/2}$ level is inefficient, which induces that the intensity of red emission is lower than that of green emission for the samples with low Er^{3+} doping concentrations (3 and 5 mol%). However, the intensity of red emission is higher than that of green emission for the samples with higher Er^{3+} doping concentrations (7 and 10 mol%). In other words, there must exist different red upconversion mechanisms between low and high Er^{3+} doping concentrations for Er^{3+}-doped $Y_2Ti_2O_7$ nanocrystals. In addition, the relative intensity ratio $[(I_G+I_R)/I_{IR}]$ of Vis and IR emissions increases from ~0.01 to an approximately value of 0.07 with the increase of Er^{3+} doping concentrations from 3 to 10 mol%. The intensified upconversion luminescence and suppressed Stokes emission is attributed to the enhanced energy transfer between Er^{3+}–Er^{3+} ions.

In order to investigate the possible up-converted emission mechanisms, we study the variation of the up-converted PL intensity by different excitation power (P) for the Er^{3+}-doped

$Y_2Ti_2O_7$ nanocrystals with low and high Er^{3+} doping concentrations. For the Er^{3+} (5 or 10 mol%)-doped $Y_2Ti_2O_7$ nanocrystals annealed at 800 °C/1 h, the intensity of green and red upconversion luminescence (526, 547, and 660 nm) versus the pump power at 980 nm has been plotted in Fig. 7. The slopes of both green and red emissions for Er^{3+} (5 mol%)-doped $Y_2Ti_2O_7$ nanocrystals are approximately equal to 2 on a log–log scale during $P \leqq 210$ mW. This result confirms that green and red emissions belong to a two-photon absorption upconversion process [40–42]. However, the slopes of 526, 547, and 660 nm emissions for Er^{3+} (10 mol%)-doped $Y_2Ti_2O_7$ nanocrystals are 2.00, 1.99, and 1.80 during $P \leqq 210$ mW, respectively, indicating that the upconversion mechanism of green emission is a two-photon absorption process but red emission a little derives from the biphotonic case. Therefore, there exist some complex mechanisms for red emission. In addition, when pumping power is larger than 210 mW, intensity saturation occurs. For Er^{3+} (5 mol%)-doped $Y_2Ti_2O_7$ nanocrystals, the slopes of green (526/547 nm) and red emissions reduce to 1.05/0.79 and 0.77, respectively. On the other hand, for Er^{3+} (10 mol%)-doped $Y_2Ti_2O_7$ nanocrystals the slopes of green (526/547 nm) and red emissions also reduce to 1.39/1.17 and 0.90, respectively. The significantly reduced slope can be attributed to the competition between linear decay and upconversion process for the depletion of the intermediate excited states [43]. Similar phenomenon is also found in the $Er_3Al_5O_{12}$ [44], Er^{3+}-doped Y_2O_3 [45], or Er^{3+}-doped $BaTiO_3$ [46].

Schematic possible upconversion mechanisms of the Er^{3+} excited-state absorption (ESA), energy-transfer upconversion (ETU), and cross-relaxation (CR) under 980 nm pumping for low and high Er^{3+} doping concentrations are shown in Fig. 8(a) and (b). Generally, there are two kinds of mechanisms for the upconversion luminescence. One is the ESA and the other is the ETU [47–49]. Mechanism I is the general ESA mechanism. A 980 nm photon elevates an electron from the $^4I_{15/2}$ level up to the $^4I_{11/2}$ level and successively the electron in the $^4I_{11/2}$ level can be excited further to the $^4F_{7/2}$ level by another 980 nm photon, which results in the green and weaker red emissions. Mechanism II is another kind of the ESA mechanism. The electron in this $^4I_{11/2}$ level relaxes to the $^4I_{13/2}$ level through a multiphonon relaxation and then the $^4F_{9/2}$ level is populated via the ESA of the electron in the $^4I_{13/2}$ level, which leads to the red emission. Mechanism III is the general ETU mechanism related to the energy transfer

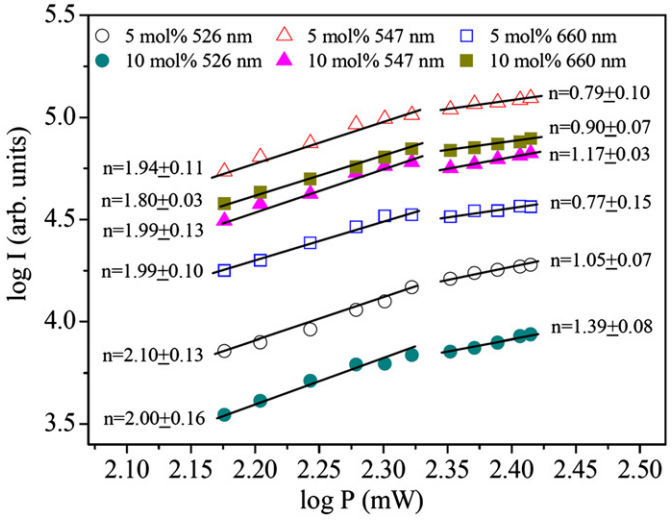

Fig. 7. Intensity of both green and red upconversion luminescence versus the pump power for the Er^{3+} (5 and 10 mol%)-doped $Y_2Ti_2O_7$ nanocrystals annealed at 800 °C/1 h.

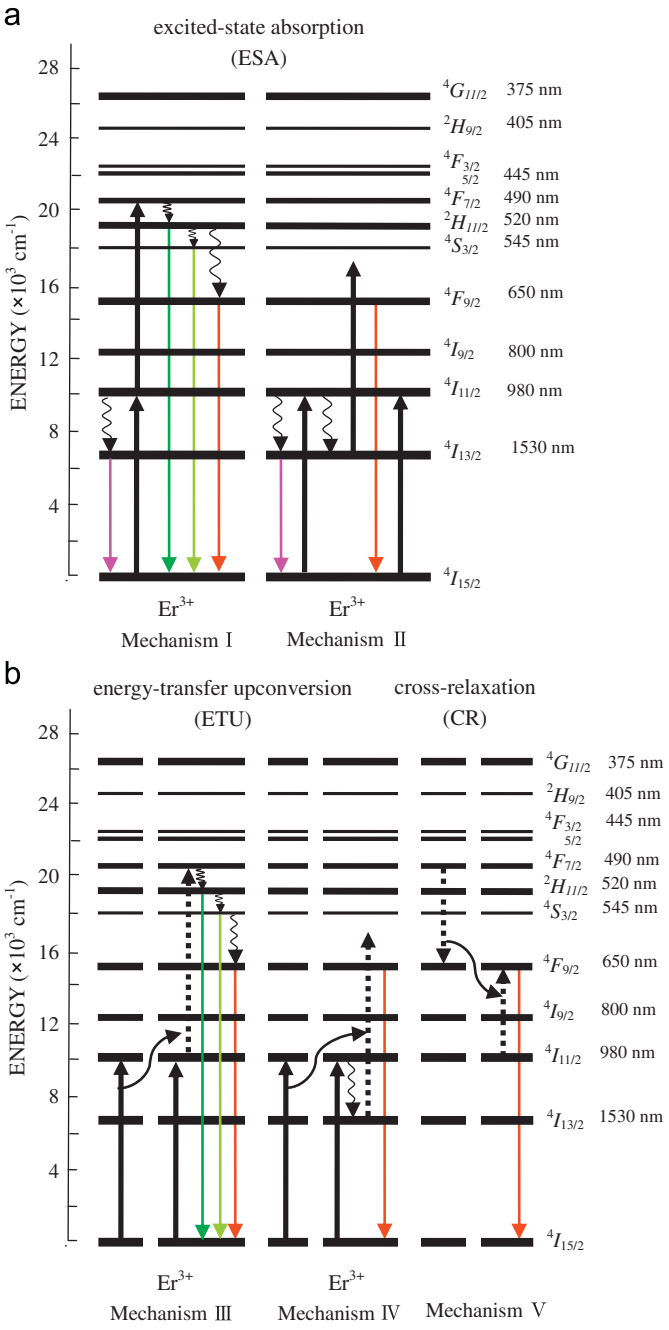

Fig. 8. Schematic possible upconversion mechanisms of (a) the Er^{3+} excited-state absorption for low Er^{3+} doping concentrations and (b) energy-transfer upconversion and cross-relaxation for high Er^{3+} doping concentrations under 980 nm pumping.

between two Er^{3+} activators. The electron of one Er^{3+} activator absorbing one 980 nm photon is elevated to the $^4I_{11/2}$ level. Then this excited electron which absorbs another 980 nm energy transferred from another neighboring Er^{3+} activator is further elevated to the $^4F_{7/2}$ level, which causes the green and weaker red emissions. Mechanism IV is another kind of the ETU mechanism. The electron of one Er^{3+} activator in the $^4I_{11/2}$ level relaxes to the $^4I_{13/2}$ level through a multiphonon relaxation and this electron in the $^4I_{13/2}$ level is elevated to the $^4F_{9/2}$ level via the excited state absorption of 980 nm energy transferred from another neighboring Er^{3+} activator, which induces the red emission. Mechanism V is a CR mechanism ($^4F_{7/2}+{}^4I_{11/2} \rightarrow {}^4F_{9/2}+{}^4F_{9/2}$). The electron of one

Er^{3+} activator in the $^4F_{7/2}$ level is de-excited to the $^4F_{9/2}$ level accompanied with raising the electron of another neighboring Er^{3+} activator from the $^4I_{11/2}$ level to the $^4F_{9/2}$ level through a CR mechanism, resulting in the red emission [50].

In the Er^{3+}-doped $Y_2Ti_2O_7$ nanocrystals with low Er^{3+} doping concentration (5 mol%), the green and red luminescence intensities present a quadratic dependence on 980 nm pump intensity, which can be ascribed to the upconversion process of the two-photon ESA involving mechanism I and II, as shown in Fig. 8(a). Although mechanism I can produce stronger green emission and weaker red emission, mechanism II can also produce additional red emission.

On the other hand, for the Er^{3+}-doped $Y_2Ti_2O_7$ nanocrystals with high Er^{3+} doping concentration (10 mol%), other mechanism III, IV, or V can also appear to be involved in the green and red luminescence except above-mentioned mechanism I and II, as shown in Fig. 8(b). Because the Er^{3+}–Er^{3+} distance is reduced for high Er^{3+} doping concentration, the cooperative effect of the ETU (mechanism III and IV) and CR (mechanism V) between two Er^{3+} ions can be enhanced. The green emission comes from the two-photon ESA (mechanism I) and ETU (mechanism III) , resulting in a slope of 2; however, the red emission involves other more complicated mechanisms such as mechanisms III, IV, and V, resulting in a slope of 1.80. Therefore, the final obtained red upconversion could be summarized from the overall contributions of five mechanisms (I, II, III, IV, and V), which makes Er^{3+} (10 mol%)-doped $Y_2Ti_2O_7$ nanocrystals generate the stronger red emission. In addition, the effects of ETU and energy migration can also suppress 1528 nm PL, and reduce its lifetime.

4. Conclusions

Er^{3+} (3, 5, 7, or 10 mol%)-doped $Y_2Ti_2O_7$ nanocrystals were fabricated by the sol–gel method. The evolutions of the phase development, crystallinity, and grain sizes between the Er^{3+} (3, 5, 7, or 10 mol%)-doped $Y_2Ti_2O_7$ nanocrystals annealed at 600–1000 °C/1 h appeared to be very similar. Below 800 °C, all samples possess the amorphous structure but after ≧800 °C annealing, all samples exhibit the well-crystallized pyrochlore structure. The average crystal sizes increase from ~70 to ~180 nm under 800–1000 °C annealing for 1 h.

The Er^{3+}-doped $Y_2Ti_2O_7$ nanocrystals absorbing the 980 nm photons can produce the upconversion (526, 547, and 660 nm; $^2H_{11/2}\rightarrow{}^4I_{15/2}$, $^4S_{3/2}\rightarrow{}^4I_{15/2}$ and $^4F_{9/2}\rightarrow{}^4I_{15/2}$, respectively) and Stokes (1528 nm; $^4I_{13/2}\rightarrow{}^4I_{15/2}$) photoluminescence. The optimum parameters for obtaining the maximum Vis and IR PL intensities of Er^{3+}-doped $Y_2Ti_2O_7$ nanocrystals is 5 mol% Er^{3+} doping concentration and 800 °C annealing temperature. The lifetimes of 547, 660, and 1528 nm PL emissions are 713 μs, 895 μs, and 4.5 ms, respectively, for 5 mol% Er^{3+} doping concentration, and the lifetimes of 547, 660, and 1528 nm PL emissions are 708 μs, 870 μs, and 2.8 ms, respectively, for 10 mol% Er^{3+} doping concentration. In addition, the IR PL decay curve is single-exponential for 5 mol% Er^{3+} doping concentration but slightly nonexponential for 10 mol% Er^{3+} doping concentration. The shorter lifetime and slightly nonexponential decay curve of Er^{3+} (10 mol%)-doped $Y_2Ti_2O_7$ nanocrystals indicate that the reduced Er^{3+}–Er^{3+} distance induces the concentration quenching effect and the local environments of Er^{3+} ions are a little different.

The Er^{3+} (5 mol%)-doped $Y_2Ti_2O_7$ nanocrystals excited by 980 nm can emit both green and red light via the two-photon excited-state absorption mechanism. For Er^{3+} (10 mol%)-doped $Y_2Ti_2O_7$ nanocrystals, the green emission comes from both the two-photon excited-state absorption and energy-transfer upconversion mechanisms but the mechanism of red emission also involves the cross-relaxation which is enhanced by the reduced distance between Er^{3+}–Er^{3+} ions except the two-photon excited-state absorption and energy-transfer upconversion mechanisms.

Acknowledgment

The authors would like to thank the National Science Council of the Republic of China for financially supporting this research under Contract no. NSC 96-2221-E-194-042-MY2.

References

[1] T. Miya, Y. Terunuma, T. Hosaka, T. Miyashita, Electron. Lett. 15 (1979) 106–108.
[2] G.Y. Chen, Y. Liu, Z.G. Zhang, B. Aghahadi, G. Somesfalean, Q. Sun, F.P. Wang, Chem. Phys. Lett. 448 (2007) 127–131.
[3] A. Shalav, B.S. Richards, M.A. Green, Sol. Energy Mat. Sol. C 91 (2007) 829–842.
[4] A. Shalav, B.S. Richards, T. Trupke, K.W. Krämer, H.U. Güdel, Appl. Phys. Lett. 86 (2005) 013505-1-013505-3.
[5] T. Trupke, A. Shalav, B.S. Richards, P. Würfel, M.A. Green, Sol. Energy Mater. Sol. C. 90 (2006) 3327–3338.
[6] T. Trupke, M.A. Green, P. Würfel, J. Appl. Phys. 92 (2002) 4117–4122.
[7] S.T. Bailey, G.E. Lokey, M.S. Hanes, J.D.M. Shearer, J.B. McLafferty, G.T. Beaumont, T.T. Baseler, J.M. Layhue, D.R. Broussard, Y.Z. Zhang, B.P. Wittmershaus, Sol. Energy Mater. Sol. C. 91 (2007) 67–75.
[8] X.Y. Huang, Q.Y. Zhang, J. Appl. Phys. 105 (2009) 053521-1-053521-4.
[9] V. Švrček, A. Slaoui, J.C. Muller, Thin Solid Films 451-452 (2004) 384–388.
[10] W.G.J.H.M. van Sark, A. Meijerink, R.E.I. Schropp, J.A.M. van Roosmalen, E.H. Lysen, Sol. Energy Mater. Sol. C. 87 (2005) 395–409.
[11] A. Schüler, M. Python, M. Valle del Olmo, E. de Chambrier, Sol. Energy 81 (2007) 1159–1165.
[12] B.S. Richards, Sol. Energy Mater. Sol. C. 90 (2006) 2329–2337.
[13] C.B. Layne, W.H. Lowdermilk, M.J. Weber, Phys. Rev. B 16 (1977) 10–20.
[14] F. Vetrone, J.C. Boyer, J.A. Capobianco, A. Speghini, M. Bettinelli, Chem. Mater. 15 (2003) 2737–2743.
[15] J.A. Capobianco, F. Vetrone, J.C. Boyer, A. Speghini, M. Bettinelli, J. Phys. Chem. B 106 (2002) 1181–1187.
[16] G.Y. Chen, H.J. Liang, H.C. Liu, G. Somesfalean, Z.G. Zhang, J. Appl. Phys. 105 (2009) 114315-1-114315-5.
[17] H. Guo, N. Dong, M. Yin, W. Zhang, L. Lou, S. Xia, J. Phys. Chem. B 108 (2004) 19205–19209.
[18] A. Patra, C.S. Friend, R. Kapoor, P.N. Prasad, Appl. Phys. Lett. 83 (2003) 284–286.
[19] E. De la Rosa, L.A. Diaz-Torres, P. Salas, R.A. Rodríguez, Opt. Mater. 27 (2005) 1320–1325.
[20] H. Xu, Z. Jiang, Chem. Phys. 287 (2003) 155–159.
[21] R. Scheps, IEEE J. Quantum Electron. 31 (1995) 309–316.
[22] J. Lian, J. Chen, L.M. Wang, R.C. Ewing, J. Matt Farmer, L.A. Boatner, K.B. Helean, Phys. Rev. B 68 (2003) 134107-1-134107-9.
[23] S.W. Han, J.S. Gardner, C.H. Booth, Phys. Rev. B 69 (2004) 024416-1-024416-7.
[24] L.M. Ershova, B.V. Ignat'ev, L.P. Kusalova, E.E. Lomonova, V.I. Myzina, V.M. Tatarintsev, L.G. Shcherbakova, Inorg. Mater. 13 (1977) 1634–1636.
[25] H.C. Gupta, S. Brown, J. Phys. Chem. Solids 64 (2003) 2205–2207.
[26] M. Hamoumi, M. Wiegel, G. Blasse, J. Solid State Chem. 108 (1994) 410–412.
[27] A.F. Fuentes, K. Boulahya, M. Maczka, J. Hanuza, U. Amador, Solid State Sci. 7 (2005) 343–353.
[28] L. Yang, T. Lu, H. Xu, W. Zhang, B. Ma, J. Appl. Phys. 107 (2010) 064903-1-064903-8.
[29] ASTM JCPDS File No. 42-0413 ($Y_2Ti_2O_7$), 1997.
[30] Y. Takahashi, S. Okada, R.B.H. Tahar, K. Nakano, T. Ban, Y. Ohya, J. Non-Cryst. Solids 218 (1997) 129–134.
[31] M.J. Weber, Phys. Rev. 171 (1968) 283–291.
[32] L.A. Riseberg, H.W. Moos, Phys. Rev. 174 (1968) 429–438.
[33] C.C. Ting, S.Y. Chen, H.Y. Lee, J. Appl. Phys. 94 (2003) 2102–2109.
[34] M. Langlet, C. Coutier, J. Fick, M. Audier, W. Meffre, B. Jacquier, R. Rimet, Opt. Mater. 16 (2001) 463–473.
[35] X. Orignac, D. Barbier, X.M. Du, R.M. Almeida, O. McCarthy, E. Yeatman, Opt. Mater. 12 (1999) 1–12.
[36] M. Carrada, F. Gourbilleau, C. Dufour, M. Levalois, R. Rizk, Opt. Mater. 27 (2005) 915–919.
[37] M. Langlet, P. Jenouvrier, R. Rimet, J. Fick, Opt. Mater. 25 (2004) 141–147.
[38] P. Jenouvrier, J. Fick, M. Audier, M. Langlet, Opt. Mater. 27 (2004) 131–137.
[39] P. Jenouvrier, M. Langlet, R. Rimet, J. Fick, Appl. Phys. A 77 (2003) 687–692.
[40] F. Vetrone, J.C. Boyer, J.A. Capobianco, J. Phys. Chem. B 107 (2003) 10747–10752.
[41] X. Qiao, X. Fan, J. Wang, M. Wang, J. Appl. Phys. 99 (2006) 074302-1-074302-8.
[42] D. Mariano da Silva, L.R.P. Kassab, S.R. Lüthi, C.B. de Araújo, A.S.L. Gomes, M.J.V. Bell, Appl. Phys. Lett. 90 (2007) 081913-1-081913-3.

[43] M. Pollnau, D.R. Gamelin, S.R. Lüthi, H.U. Güdel, M.P. Hehlen, Phys. Rev. B 61 (2000) 3337–3346.
[44] G.S. Maciel, N. Rakov, M. Fokine, I.C.S. Carvalho, C.B. Pinheiro, Appl. Phys. Lett. 89 (2006) 081109-1-081109-3.
[45] X. Qin, T. Yokomori, Y. Ju, Appl. Phys. Lett. 90 (2007) 073104-1-073104-3.
[46] P. Ghosh, S. Sadhu, T. Sen, A. Patra, Bull. Mater. Sci. 31 (2008) 461–465.
[47] P. Blixt, J. Nilsson, T. Carlinäs, B. Jaskorzynska, IEEE. Photonic Technol. Lett. 3 (1991) 996–998.
[48] F. Auzel, Chem. Rev. 104 (2004) 139–173.
[49] M.P. Hehlen, G. Frei, H.U. Güdel, Phys. Rev. B 50 (1994) 16264–16273.
[50] A. Walasek, E. Zych, J. Zhang, S. Wang, J. Lumin. 127 (2007) 523–530.